# An uncommon $[K^+(Mg^{2+})_2]$ metal ion triad imparts stability and selectivity to the Guanidine-I riboswitch

ROBERT J. TRACHMAN III and ADRIAN R. FERRÉ-D'AMARÉ

Biochemistry and Biophysics Center, National Heart, Lung, and Blood Institute, Bethesda, Maryland 20892-8012, USA

## ABSTRACT

**The widespread *ykkC*-I riboswitch class exemplifies divergent riboswitch evolution. To analyze how natural selection has diversified its versatile RNA fold, we determined the X-ray crystal structure of the *Burkholderia sp. TJI49 ykkC*-I subtype-1 (Guanidine-I) riboswitch aptamer domain. Differing from the previously reported structures of orthologs from *Dickeya dadantii* and *Sulfobacillus acidophilus*, our *Burkholderia* structure reveals a chelated $K^+$ ion adjacent to two $Mg^{2+}$ ions in the guanidine-binding pocket. Thermal melting analysis shows that $K^+$ chelation, which induces localized conformational changes in the binding pocket, improves guanidinium-RNA interactions. Analysis of ribosome structures suggests that the $[K^+(Mg^{2+})_2]$ ion triad is uncommon. It is, however, reminiscent of metal ion clusters found in the active sites of ribozymes and DNA polymerases. Previous structural characterization of *ykkC*-I subtype-2 RNAs, which bind the effector ligands ppGpp and PRPP, indicate that in those paralogs, an adenine responsible for $K^+$ chelation in the *Burkholderia* Guanidine-I riboswitch is replaced by a pyrimidine. This mutation results in a water molecule and $Mg^{2+}$ ion binding in place of the $K^+$ ion. Thus, our structural analysis demonstrates how ion and solvent chelation tune divergent ligand specificity and affinity among *ykkC*-I riboswitches.**

**Keywords: evolution; guanidine; potassium; riboswitch; structure**

## INTRODUCTION

Riboswitches are structured RNA elements that evolved to regulate gene expression through binding of small molecules (Roth and Breaker 2009; Serganov and Nudler 2013). A compelling example highlighting the divergent evolution of riboswitches and their acquisition of different specificities is the *ykkC*-I riboswitch class (Nelson et al. 2017; Sherlock et al. 2018a,b). *ykkC*-I is widespread among bacterial phyla (e.g., Actinobacteria, Firmicutes, Proteobacteria, and Cyanobacteria). This riboswitch class is comprised of five subtypes (subtype 1, subtypes 2a–2d), which control disparate metabolic pathways using a nearly identical RNA fold (Battaglia et al. 2017; Reiss et al. 2017; Knappenberger et al. 2018; Peselis and Serganov 2018). The effector ligands for these subtypes vary in both chemical structure and cellular function (subtype 1 [guanidine], 2a [ppGpp] 2b [PRPP], 2c [{d}NDP], 2d [unknown]). The structural dissimilarity between *ykkC*-I effector ligands has reinforced the notion that this RNA may reside within a privileged class (Hallberg et al. 2017; Page et al. 2018) of RNA molecules. Thus, these RNAs are amenable to mutations in the binding pocket to enable tuning of ligand specificity and affinity while maintaining global architecture and regulatory function. Indeed, paired elements 1 and 3 of the *ykkC*-I fold (Fig. 1A) can be swapped between subtypes to change ligand specificity with only modest decrease in ligand affinity (Knappenberger et al. 2020).

Structures have been determined for members of each of the *ykkC*-I riboswitch subtypes, with the exception of the orphan *ykkC*-I-2d subtype (Battaglia et al. 2017; Reiss et al. 2017; Knappenberger et al. 2018; Peselis and Serganov 2018). Those structures reveal a conserved global architecture with varying sequences in paired elements, and an optional paired element in the vicinity of the ligand binding pocket. The most common effector ligand for *ykkC*-I riboswitches is guanidine, with subtype-1 (Guanidine-I) comprising 75% of all known *ykkC*-I examples, and being observed in the most diverse phyla. To further understand how RNA structure is molded by natural selection, we solved the X-ray crystal structure of the *Burkholderia sp. TJI49* Guanidine-I riboswitch. Structural comparison to two previously characterized Guanidine-I riboswitch variants from *D. dadantii* (Battaglia et al. 2017) and *S. acidophilus* (Reiss et al. 2017) reveal differences in both overall global architecture and core binding-pocket structure. The most notable difference is the chelation of a $K^+$

**Corresponding author: robert.trachman@nih.gov**

Article is online at http://www.rnajournal.org/cgi/doi/10.1261/rna.078824.121.

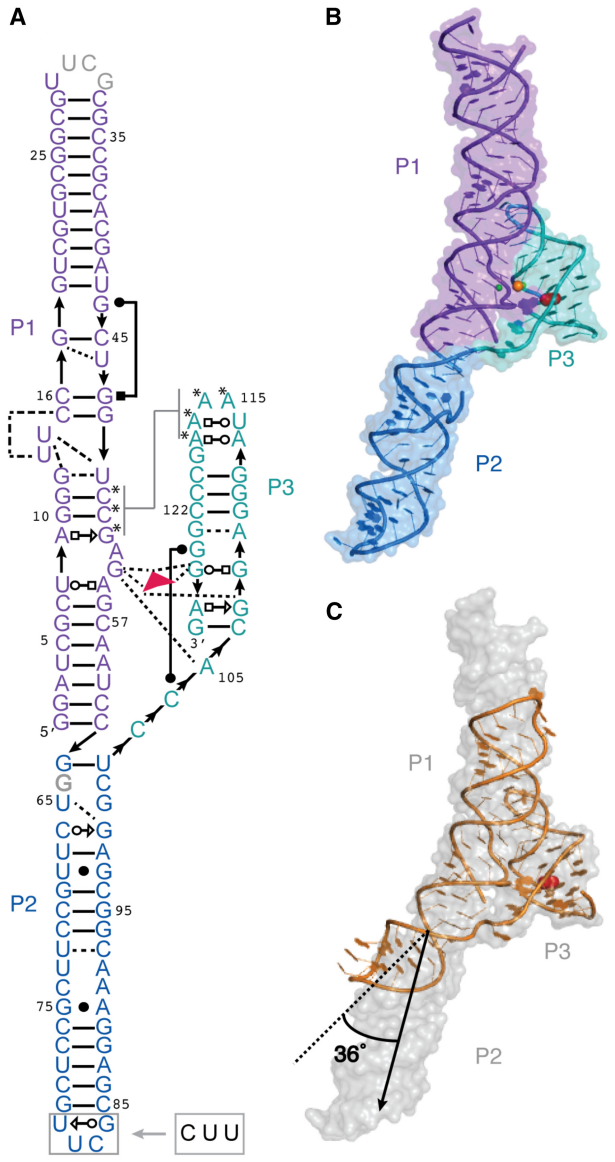


**FIGURE 1.** Overall structure of the *Burkholderia* Guanidine-I riboswitch. (*A*) Secondary structure. Thin lines with arrowheads denote connectivity. Base pairs are represented with Leontis–Westhof symbols (Leontis and Westhof 2001). Single hydrogen bonds are represented as dashed lines. Red triangle denotes bound guanidine. Asterisks denote residues that participate in A-minor interaction. Wild-type and crystallization construct sequences of the terminal loop of P2 are boxed and blue, respectively. Disordered residues are shown in gray. (*B*) Cartoon representation of the three-dimensional structure with van der Waals surface of the RNA. Green, yellow, and red spheres denote $Mg^{2+}$, $K^+$, and guanidine, respectively. (*C*) Van der Waals surface of the *Burkholderia* Guanidine-I riboswitch (gray) superimposed with *D. dadantii* Guanidine-I riboswitch (cartoon; orange). Dashed and solid lines depict the P2 helical axes of *D. dadantii* and *Burkholderia*, respectively.

ion by conserved nucleotides adjacent to the guanidine binding pocket. This $K^+$ ion participates in a metal ion triad with two adjacent $Mg^{2+}$ ions. Thermal melting analyses demonstrate that the ligand bound *Burkholderia sp. TJI49* Guanidine-I riboswitch is preferentially stabilized by the monovalent ion $K^+$ relative to $Na^+$. The $[K^+(Mg^{2+})_2]$ metal ion triad appears to be uncommon in RNA, although it has been reported (Nakamura et al. 2012; Freudenthal et al. 2013) in the active site of some DNA polymerases.

## RESULTS

### Overall structure of the *Burkholderia* Guanidine-I riboswitch

The crystal structure of the *Burkholderia* Guanidine-I riboswitch was solved using the molecular replacement method (Materials and Methods, Fig. 1A,B; Supplemental Table 1). Our crystals of this RNA diffract X-rays to ~2.4 Å resolution (refinement was limited to 2.7 Å), and contain one RNA molecule in the crystallographic asymmetric unit. Overall, the aptamer domain is comprised of three helices (paired elements P1–P3). P1 and P2 form a ~136 Å-long helical stack (Fig. 1B; Supplemental Fig. 1). A long-range tertiary-interaction is formed through an A-minor motif composed of four conserved adenines in the stem–loop of P3 and three bases in P1. The guanidine binding-pocket is formed at the P1–P3 interface below the A-minor motif. Here, a two-residue bulge in P1 extends into the vicinity of P3 to form the guanidine binding-pocket. The *Burkholderia* Guanidine-I riboswitch contains an internal loop in P2 which imparts a 36° bend relative to the helical axis (Fig. 1C). The P2 internal loop forms a poorly resolved triplex between residues U65, C66, and G99.

### Guanidinium recognition by the *Burkholderia* riboswitch

An oblong feature in the unbiased residual electron density map near the highly conserved residues G54, A55, G107, and G125 (Fig. 2A,B) was modeled as a bound guanidinium. The guanidinium interacts with the RNA on all three of its edges and one of its two faces. The ligand stacks on the nucleobase of G107. The guanidinium is coplanar with G125, whose Hoogsteen edge makes two hydrogen bonds with amines of the ligand. Two additional hydrogen bonds are formed between the guanidinium and the *pro-*$R_P$ oxygen and 05′ of G108. Compared to previously reported Guanidine-I riboswitch structures, these four hydrogen bonds are more closely coplanar with the $sp^2$-hybridized ligand, and appear to impose a slight tilt to the guanidinium toward the conserved residues G54 and A55. Here, the edge of guanidinium participates in two dipole–dipole interactions with O6 of G54 and N1 of A55. Overall, these interactions impart selectivity for guanidinium over urea through cation-π, hydrogen bond, and dipole interactions. The conserved binding pocket bases

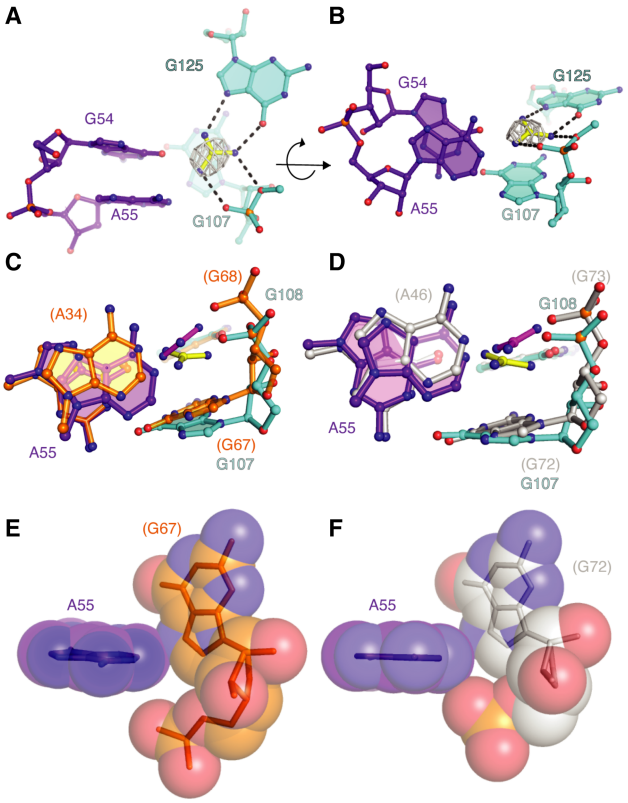


**FIGURE 2.** Guanidine-binding pocket structure. (*A*) The *Burkholderia ykkC*-I guanidine-binding pocket, colored as in Figure 1. Gray mesh depicts portion of the $|F_o|-|F_c|$ electron density map, prior to ligand modeling, contoured at 2.0σ. Hydrogen bonds are depicted as black dashed lines. Bound guanidine is shown in yellow ball-and-stick representation. (*B*) 80° rotation of *A*. (*C*) Structural superposition of *Burkholderia* residues on the corresponding *D. dadantii* binding pocket (RNA, orange; guanidine, magenta). Residue numbers in parentheses correspond to PDB ID 5U3G (Battaglia et al. 2017). (*D*) Structural superposition on the *S. acidophilus* binding pocket (RNA, gray; guanidine, magenta). Residue numbers in parentheses correspond to PDB ID 5T83 (Reiss et al. 2017). Structural superpositions were performed for all non-hydrogen atoms, with residues 20–41 and 63–102 of the *Burkholderia* RNA omitted. (*E*) Van der Waals representation of A55 from *Burkholderia ykkC*-I and G67 from *D. dadantii* Guanidine-I. (*F*) Van der Waals representation of A55 from *Burkholderia ykkC*-I and G72 from *S. acidophilus* Guanidine-I.

of the RNA would also discriminate sterically against alkylated derivatives of guanidinium, such as arginine.

The ligand-binding site of the *Burkholderia* Guanidine-I riboswitch differs subtly but consistently from those of its *D. dadantii* and *S. acidophilus* orthologs. After overall superposition of the RNAs, root-mean-square differences (r.m.s.d.) for all non-hydrogen atoms of the guanidinium and binding-pocket residues G54, A55, G107, and G108 are 1.1 and 0.9 Å versus the corresponding atoms of the *D. dadantii* and *S. acidophilus* riboswitches, respectively. While G54 and G125 are in indistinguishable positions in the three RNAs, A55, G107, and G108 (*Burkholderia* numbering) are not (Fig. 2C,D). In the new structure, the three residues shift relative to the base plane of G125 by ~1.1 Å, and the base of A55 rotates toward its sugar edge. Concomitantly, the base of G107, with which it is in van der Waals contact, shifts. This is evident in the superimposed structures, where the base planes of G107 (*Burkholderia*) and the corresponding G67 and G72 (*D. dadantii* and *S. acidophilus* numbering, respectively) are offset by 22° and 16°, respectively (Fig. 2C,D) to relieve steric clash (Fig. 2E,F). Because the bound guanidinium stacks on the nucleobase of G107, the plane of the bound ligand differs between the *Burkholderia* complex and those of *D. dadantii* and *S. acidophilus* by 46° and 45°, respectively. This structural rearrangement improves cation-π interaction between the ligand and G107; the interplane distances shrink from 4.1 Å (*D. dadantii*) and 3.8 Å (*S. acidophilus*), to 3.4 Å in the *Burkholderia* structure.

## A $[K^+(Mg^{2+})_2]$ triad in the ligand binding site

Below the A-minor motif, two bulges from the paired elements P1 and P3 come into close proximity. As observed in the *D. dadantii* and *S. acidophilus* aptamer domain cocrystal structures, two metal ions are coordinated at this interface. $M_A$, which is modeled as $Mg^{2+}$, is coordinated by the *pro*-$S_p$ nonbridging phosphate oxygen (n.b.p.o) of A53 and the *pro*-$S_p$ n.b.p.o of C120 with distances of 2.05 and 2.45 Å, respectively (Fig. 3A,B). The coordination network of $M_A$ forms an angle of 79°. The second metal ion, $M_B$ (also modeled as $Mg^{2+}$), is coordinated by the *pro*-$R_p$ n.b.p.o of C120 (1.98 Å), the *pro*-$S_p$ n.b.p.o of G119 (2.57 Å), and the *pro*-$R_p$ n.b.p.o of A53 (2.41 Å), with interatomic angles of 91°, 90°, and 74°. All of these values are within the range of distances and angles expected for $Mg^{2+}$ chelation at a coordinate precision of 0.37 Å (Auffinger et al. 2020) and the assignment of magnesium to $M_A$ and $M_B$ is consistent with the higher resolution cocrystal structure of the *D. dadantii* ortholog.

Unexpectedly, in the *Burkholderia* structure, an electron density feature consistent with a third metal ion ($M_C$) is present in the vicinity of $M_A$ and $M_B$. $M_C$ is within coordination distance from five ligands: the *pro*-$R_p$ n.b.p.o of A53 (3.1 Å), the *pro*-$S_p$ n.b.p.o of G119 (2.9 Å), the 2′-OH of A53 (2.5 Å), the O3′ of A53 (3.2 Å), and the N7 of A55 (3.4 Å). The coordination geometry of $M_C$ most closely resembles incomplete heptacoordination. On the basis of this, the coordination distances, the refined *B*-factors (Zheng et al. 2017; Auffinger et al. 2020), and residual difference Fourier synthesis features after alternative refinements modeling the feature as any of the metal ions in the crystallization solution (Supplemental Fig. 2), we have modeled $M_C$ as $K^+$. Superposition of the three Guanidine-I riboswitch structures yields good overlay of $M_A$ and $M_B$ (Fig. 3C,D). However, chelation of $M_C$ results in a displacement of the nucleobase of A55 (r.m.s.d. 1.2 Å relative to either of the

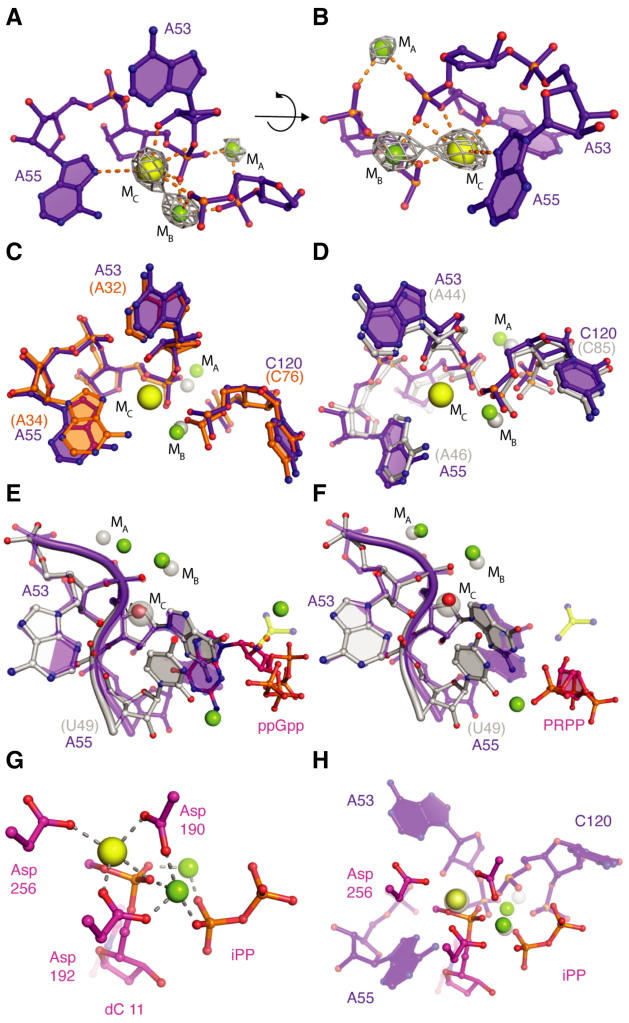


**FIGURE 3.** Structural analysis of the metal-ion triad. (*A*) Metal ion network in *Burkholderia* Guanidine-I riboswitch. $|F_o|-|F_c|$ electron density map, prior to ion modeling, contoured at 3.2σ (gray mesh). Modeled $Mg^{2+}$ (green, $M_A$ and $M_B$) and $K^+$ (yellow, $M_C$). Orange dashed lines denote metal ion coordination. (*B*) 160° rotation of *A*. (*C*) Structural superposition of *D. dadantii* $Mg^{2+}$ cluster (RNA, orange; ion, gray). (*D*) Structural superposition of *S. acidophilus* $Mg^{2+}$ cluster (RNA and ions, gray). (*E*) Structural superposition of the *Burkholderia* Guanidine-I riboswitch ion core and binding pocket with the *S. acidophilus* ppGpp riboswitch binding pocket and ion core (PDB ID:6DMC; [Peselis and Serganov 2018]). Ions from *Burkholderia* Guanidine-I riboswitch are shown as gray transparent spheres. (*F*) Structural superposition of the *Burkholderia* Guanidine-I riboswitch ion-core and binding pocket with the *S. lipocalidus* PRPP riboswitch binding pocket and ion core (PDB ID: 6DLT [Peselis and Serganov 2018]). Ions from *Burkholderia* Guanidine-I riboswitch are shown as gray transparent spheres. (*G*) Ion cluster of the closed DNA polymerase β product complex. $Mg^{2+}$ and $Na^+$ are shown in green and yellow spheres, respectively (PDB ID: 4KLL [Freudenthal et al. 2013]). (*H*) Structural superposition of the DNA polymerase β product complex with the *Burkholderia* Guanidine-I metal-ion triad (translucent purple and gray). For RNAs superpositions between *ykkC*-I riboswitches, structural superpositions were performed for all non-hydrogen atoms with residues 20–41 and 63–102 of the *Burkholderia ykkC-I* riboswitch deleted from the search. Structural superposition of *Burkholderia ykkC-I* and DNA polymerase β product complex is centered on the three metal ions.

*D. dadantii* and *S. acidophilus* orthologs), altering the binding pocket conformation.

The *ykkC*-I subtype-2a (ppGpp) and subtype-2b (PRPP) riboswitches differ, in part, from Guanidine-I riboswitches by a transversion of A55 to uridine (U49 in *S. acidophilus* numbering). Structural studies of the ppGpp and PRPP riboswitches (Knappenberger et al. 2018; Peselis and Serganov 2018) revealed that in both of these riboswitches, U49 coordinates a water molecule in the exact location as the $K^+$ ion in the *Burkholderia* Guanidine-I structure (Fig. 3E,F). Additionally, the nucleobase of U49 coordinates a $Mg^{2+}$ ion adjacent to the equivalent location of the guanidine binding pocket in Guanidine-I (Fig. 3E,F). Our structure suggests, therefore, that mutation to uridine prevents guanidine binding to subtype-2 riboswitches not only through RNA-ligand contacts, but also altered solvent and ion interactions.

While clusters of two adjacent cations are commonly observed in structured RNAs such as the ribosome (Conn et al. 1999, 2002; Hsiao and Williams 2009), M-box riboswitch (Dann et al. 2007), NiCo riboswitch (Furukawa et al. 2015), and $Mn^{2+}$ riboswitch (Price et al. 2015; Bachas and Ferré-D'Amaré 2018), RNA-bound $[K^+(Mg^{2+})_2]$ triads are not well documented. Simulations have demonstrated long residence times for symmetric $K^+$ and $Mg^{2+}$ association sites (Auffinger et al. 2003, 2004) in locations void of metal ions in crystal structures. These reports suggest that metal ion clusters may be more common than generally appreciated. To examine how common $[K^+(Mg^{2+})_2]$ triads are, we searched for $Mg^{2+}$, $Na^+$, and $K^+$ ions that form triads with inter-ion distances shorter than 7.5 Å in a high-resolution structure (1.98 Å) of the 70S ribosome (PDB ID: 7K00 [Watson et al. 2020]). Manual curation of the output of our algorithm for identifying ions that make at least two RNA contacts with electronegative groups yielded no metal ion triads. Biochemical evidence for three-metal ion catalysis has been reported for the *Tetrahymena* ribozyme (Shan et al. 1999). Despite a lack of structural corroboration for those results, a similar three-metal ion catalytic network has been observed in the product states of DNA polymerases η and β (Nakamura et al. 2012; Freudenthal et al. 2013). Like the Guanidine-I riboswitch, the product state of DNA polymerase β also coordinates two divalent ions and a monovalent ion (Fig. 3G). Structural superposition of the chelated ions and coordinating atoms from DNA Pol. β and the Guanidine-I riboswitch shows striking similarity (Fig. 3H; r.m.s.d. = 0.9 Å). This suggests that $[K^+(Mg^{2+})_2]$ triads, while uncommon, are integral structural features of biomolecules.

## Thermal melting analysis supports role of $K^+$

Thermal melting can indicate whether specific, chelated, ions stabilize the tertiary structure of an RNA (Shiman and Draper 2000; Lambert et al. 2009). To test if $K^+$

participates in forming the ligand-bound structure of the *Burkholderia* riboswitch aptamer domain, we determined its melting profiles in the presence of $K^+$ or $Na^+$, with varying concentration of guanidinium or urea (Fig. 4A–E). Folded, structured RNAs exhibit biphasic thermal melting profiles when plotted as the derivative of UV absorbance versus temperature. The first transition corresponds to the unfolding of tertiary structure, while the second corresponds to the melting of the secondary structure. In the absence of ligand or presence of urea, the Guanidine-I riboswitch exhibits only secondary structure melting (Fig. 4A,B). Addition of as little as 50 µM guanidinium produces a biphasic thermal melting profile, but only in the presence of $K^+$. The midpoint of this thermal transition ($T_m$) increases with increased guanidinium concentration (Fig. 4C–E). While a weak phase transition is suggested by melting in the presence of $Na^+$ at the highest guanidinium concentration (Fig. 4E), a gaussian fit did not converge on a solution using these data, and therefore a $T_m$ could not be determined. These results support the existence of a specific $K^+$ chelation site that is thermodynamically linked to guanidinium binding in the *Burkholderia* riboswitch aptamer domain.

## DISCUSSION

The Guanidine-I riboswitch is one of four known riboswitch classes that respond to guanidinium (Nelson et al. 2017; Sherlock and Breaker 2017; Sherlock et al. 2017; Lenkeit et al. 2020; Salvail et al. 2020), and is also part of a larger riboswitch class, *ykkC*-I, members of which recognize their respective, distinct metabolites using a conserved RNA fold (Battaglia et al. 2017; Reiss et al. 2017; Knappenberger et al. 2018; Peselis and Serganov 2018). We now demonstrate that a Guanidine-I riboswitch chelates a $K^+$ ion adjacent to a binuclear $Mg^{2+}$ cluster in its guanidinium binding pocket. While ion chelation is commonly observed in RNA crystal structures, this $K^+$ chelation site went unrecognized in two previous crystallographic studies of orthologous Guanidine-I riboswitches (Battaglia et al. 2017; Reiss et al. 2017). The cocrystals from which those structures were derived were grown under conditions containing abundant, nonphysiological $Na^+$ as the predominant monovalent ion, and either no $K^+$ (Battaglia et al. 2017), or an unphysiologically low concentration of it (~10 mM; Reiss et al. 2017). Given the conserved sequence and structure in this region of the Guanidine-I riboswitch, and the similar resolution of all three data sets, it is likely that the differences in crystallization conditions account for the discrepancy in $K^+$ chelation.

Through thermal melting analysis, we have demonstrated that the *Burkholderia* Guanidine-I riboswitch tertiary fold is preferentially stabilized by the physiologically relevant $K^+$ ion relative to $Na^+$. While RNA tertiary structures are often stabilized to a greater extent by small, diffuse

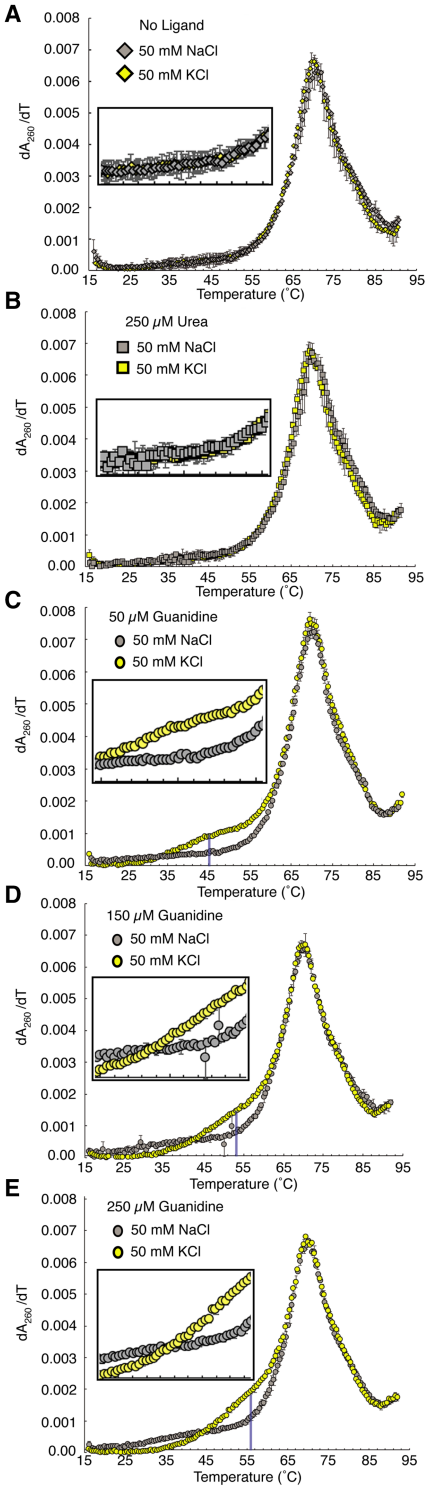


**FIGURE 4.** Thermal melting analysis of Guanidine-I riboswitch. Thermal denaturation of the *Burkholderia* Guanidine-I riboswitch was performed in the presence of 0.5 mM $MgCl_2$ and either 50 mM NaCl (gray) or 50 mM KCl (yellow) and (*A*) no ligand, (*B*) 250 µM urea, (*C*) 50 µM guanidine, (*D*) 150 µM guanidine, or (*E*) 250 µM guanidine. Error bars represent standard error of three independent measurements. Melting temperatures ($T_m$) for the tertiary structure unfolding transition ($K^+$ data only) are marked with a blue line. *Insets* show zoomed-in view of 35°C–55°C regions.

monovalent ions (i.e., $Li^+$ and $Na^+$), $K^+$ chelation can disrupt this trend to enable RNA folds with exceptionally high electrostatic potential (Lambert et al. 2009). Our results establish the stabilizing effect of $K^+$ on Guanidine-I riboswitch structure and ligand recognition. Residue A55, the nucleobase responsible for coordinating $K^+$ and altering the organization of the guanidinium binding pocket upon chelation, is mutated from an adenine to a pyrimidine in all reported *ykkC* subtype-2 examples. Consistent with our analysis, all reported structures of *ykkC* subtype-2 examples contain a water molecule in place of the chelated $K^+$ of the *Burkholderia* riboswitch, and a $Mg^{2+}$ coordinated proximally to the guanidine pocket. Just as the binding of $K^+$ molds the *Burkholderia* riboswitch binding pocket to suit guanidinium, water and $Mg^{2+}$ appear to do the same for ppGpp and PRPP riboswitches. Together, these results show how solvent and counterions can expand the ligand specificity of a single aptamer fold.

While *ykkC*-I riboswitches are structurally interesting and complex, there is no evidence to suggest that this RNA fold, or any other, is more amenable to divergent evolution than other structured RNAs. Structure-guided in vitro evolution of the *glmS* (Lau and Ferre-D'Amare 2013; Lau et al. 2017) and purine riboswitches (Porter et al. 2017) has demonstrated that even a small number of mutations can impart dissimilar ligand specificity. With as few as three mutations, the *glmS* riboswitch-ribozyme shifts selectivity from requiring glucosamine-6-phosphate (GlcN6P) for catalysis, to only requiring divalent ions ($glmS^{AAA}$ and $glmS^{Ca}$). While maintaining the same global fold, $glmS^{AAA}$ repurposes a structural divalent cation as a coenzyme and reorganizes the GlcN6P binding site to chelate a divalent ion. The $glmS^{Ca}$ variant results in a shift in the active site location so that the cleavage occurs +1 nucleotide relative to *glmS* and $glmS^{AAA}$. Much like the *glmS* riboswitch-ribozyme, *ykkC*-I riboswitches alter binding pocket locally to switch specificity. Our new structure of a member of the *ykkC*-I riboswitch class showcases how evolution can use solvent and cation interactions to tune the small molecule selectivity of an RNA through subtle changes in binding pocket organization.

## MATERIALS AND METHODS

### RNA preparation

RNA was in vitro transcribed as previously described (Trachman et al. 2020); purified by electrophoresis on a 13% polyacrylamide gel (37:1; acrylamide:bisacrylamide), 1×TBE, 8 M Urea gels; electroeluted from gel slices; washed once with 1 M KCl; and exchanged by ultrafiltration into 20 mM MOPS pH 7.0, 100 mM KCl, and 10 µM EDTA (0.1 µm cutoff, Amicon Ultrafree-MC, Millipore), and stored at −20°C.

### Crystallization and diffraction data collection

*Burkholderia* Guanidine-I riboswitch in 20 mM MOPS-KOH pH 7.0, 100 mM KCl, 10 µM EDTA was heated to 95°C for 3 min, incubated at RT for 10 min, mixed with equimolar guanidine•HCl and 5 mM $MgCl_2$, then incubated at RT for 30 min. For crystallization, 1.0 µL of RNA solution (150 µM) and 1.0 µL reservoir solution (50 mM HEPES pH 7.5, 200 mM $NH_4SO_4$, 10 mM $SrCl_2$, 30% PEG 3350, 3% isopropanol) were mixed and equilibrated at 288 K. Crystals were grown by sitting drop vapor diffusion under microbatch (1:1; silicon : paraffin oil). Large hexagonal rod-like crystals grew in 1–3 d to maximum dimensions of 600 × 200 × 200 $\mu m^3$. Additional cryoprotection was not necessary prior to mounting the crystal in a nylon loop and vitrifying by plunging into liquid nitrogen. Data were collected at 100 K at ALS Bl501 using 12.5 keV X-radiation. Data were reduced in XDS (Kabsch 2010) with 10% of reflections flagged for $R_{Free}$ calculation. Data collection statistics are summarized in Supplemental Table 1.

### Structure determination and refinement

The *Burkholderia* Guanidine-I riboswitch structure was solved by molecular replacement using the program Phaser (McCoy et al. 2007). The *S. acidophilus* Guanidine-I structure (PDB ID: 5T83), with nonconserved residues, the guanidine ligand, and all ions deleted, was used as the search model. The top solution had a TFZ score of 20.2. Multiple rounds of manual building and refinement were performed in Coot and Phenix.refine, respectively. Electron density for residues 31–33 was poorly defined; however, positive electron density features were observed that were modeled as inorganic phosphate and are likely part of the RNA backbone. Simulated annealing was performed every six refinement cycles at 4000 K until an $R_{Free}$ of 0.32 was reached. Refinement statistics are summarized in Supplemental Table 1.

### Small angle X-ray scattering

SAXS experiments were performed at beamline 12-ID-B of The Advanced Photon Source at Argonne National Laboratories. Samples were prepared and purified by size-exclusion chromatography as described previously (Jeng et al. 2021), with the exception of $MgCl_2$ being supplied in 2.5 mM. Samples, ranging in concentration from 0.25–0.9 mg/mL, were passed through a flow cell upon which they were exposed to X-rays (12 keV) for 1.0 sec, followed by a 1.0 sec rest time. Forty data sets were collected per sample using a Pilatus 2M detector positioned at 3.6 m from the sample capillary. Prior to averaging, each data set was examined for radiation damage and aggregation using Igor Pro (WaveMetrics). Guinier analysis was performed using Igor Pro. Indirect Fourier transformation was performed using the programs DATGNOM and GNOM (Petoukhov and Svergun 2007).

### Thermal melts

Thermal melts were performed as previously described (Trachman and Draper 2013). Briefly, thermal denaturation was carried out on a Cary 400 spectrophotometer with temperatures monitored within a quartz cuvette. RNA samples were dissolved in 10 mM HEPES pH 7.5, 50 mM monovalent ion (either KCl or

NaCl), 0.5 mM $MgCl_2$, and stated amount of ligand (either guanidine or urea). RNA was heated to 65°C and cooled to 15°C prior to data collection. Temperature was ramped from 15°C to 95°C at 0.5°C/min. UV signals were monitored at 260 and 280 nm and collected every 30 sec. Derivative of data was taken over a five data point window and fit using Global Melt Fit (Draper et al. 2001) to determine the melting transition temperature.

## DATA DEPOSITION

Atomic coordinates and structure factors amplitudes have been deposited with the PDB under accession code 7MLW.

## SUPPLEMENTAL MATERIAL

Supplemental material is available for this article.

## ACKNOWLEDGMENTS

We thank M. Banco, D. Draper, and R. Breaker for discussions. We thank the staff of beamlines 5.0.1 and 5.0.2 of the Advanced Light Source, Lawrence Berkeley National Laboratory (ALS), 24-ID-C and 12-ID-B of the Advanced Photon Source, Argonne National Laboratory (APS) for crystallographic data collection and small-angle X-ray scattering data collection. Instrumentation and data analysis support for small-angle X-ray scattering was provided by Y.X. Wang, L. Fang, and X. Zhoa. This research used resources of the Advanced Photon Source, a U.S. Department of Energy (DOE) Office of Science User Facility operated for the DOE Office of Science by Argonne National Laboratory under contract no. DE-AC02-06CH11357. This work is based upon research conducted at the Northeastern Collaborative Access Team beamlines, which are funded by the National Institute of General Medical Sciences from the National Institutes of Health (NIH; P30 GM124165). The Pilatus 6M detector on 24-ID-C beam line is funded by a NIH-ORIP HEI grant (S10 RR029205). R.J.T. is the recipient of a K22 Career Transition Award from the National Heart, Lung, and Blood Institute, NIH (NHLBI). This work was supported by the intramural program of the NHLBI.

*Author contributions*: R.J.T. conceived the project and performed experiments. A.R.F. and R.J.T. prepared the manuscript.

*Received May 3, 2021; accepted July 5, 2021.*

## REFERENCES

Auffinger P, Bielecki L, Westhof E. 2003. The $Mg^{2+}$ binding sites of the 5S rRNA loop E motif as investigated by molecular dynamics simulations. *Chem Biol* **10:** 551–561. doi:10.1016/S1074-5521(03)00121-2

Auffinger P, Bielecki L, Westhof E. 2004. Symmetric $K^+$ and $Mg^{2+}$ ion-binding sites in the 5S rRNA loop E inferred from molecular dynamics simulations. *J Mol Biol* **335:** 555–571. doi:10.1016/j.jmb.2003.10.057

Auffinger P, Ennifar E, D'Ascenzo L. 2020. Deflating the RNA $Mg^{2+}$ bubble. Stereochemistry to the rescue! *RNA* **27:** 243–252. doi:10.1261/rna.076067.120

Bachas ST, Ferré-D'Amaré AR. 2018. Convergent use of heptacoordination for cation selectivity by RNA and protein metalloregulators. *Cell Chem Biol* **25:** 962–973. doi:10.1016/j.chembiol.2018.04.016

Battaglia RA, Price IR, Ke A. 2017. Structural basis for guanidine sensing by the *ykkC* family of riboswitches. *RNA* **23:** 578–585. doi:10.1261/rna.060186.116

Conn GL, Draper DE, Lattman EE, Gittis AG. 1999. Crystal structure of a conserved ribosomal protein-RNA complex. *Science* **284:** 1171–1174. doi:10.1126/science.284.5417.1171

Conn GL, Gittis AG, Lattman EE, Misra VK, Draper DE. 2002. A compact RNA tertiary structure contains a buried backbone-$K^+$ complex. *J Mol Biol* **318:** 963–973. doi:10.1016/S0022-2836(02)00147-X

Dann CE III, Wakeman CA, Sieling CL, Baker SC, Irnov I, Winkler WC. 2007. Structure and mechanism of a metal-sensing regulatory RNA. *Cell* **130:** 878–892. doi:10.1016/j.cell.2007.06.051

Draper DE, Bukhman YV, Gluick TC. 2001. Thermal methods for the analysis of RNA folding pathways. *Curr Protoc Nucleic Acid Chem* **Chapter 11:** Unit 11.3. doi:10.1002/0471142700.nc1103s02

Freudenthal BD, Beard WA, Shock DD, Wilson SH. 2013. Observing a DNA polymerase choose right from wrong. *Cell* **154:** 157–168. doi:10.1016/j.cell.2013.05.048

Furukawa K, Ramesh A, Zhou Z, Weinberg Z, Vallery T, Winkler WC, Breaker RR. 2015. Bacterial riboswitches cooperatively bind $Ni^{2+}$ or $Co^{2+}$ ions and control expression of heavy metal transporters. *Mol Cell* **57:** 1088–1098. doi:10.1016/j.molcel.2015.02.009

Hallberg ZF, Su Y, Kitto RZ, Hammond MC. 2017. Engineering and *in vivo* applications of riboswitches. *Annu Rev Biochem* **86:** 515–539. doi:10.1146/annurev-biochem-060815-014628

Hsiao C, Williams LD. 2009. A recurrent magnesium-binding motif provides a framework for the ribosomal peptidyl transferase center. *Nucleic Acids Res* **37:** 3134–3142. doi:10.1093/nar/gkp119

Jeng SCY, Trachman RJ III, Weissenboeck F, Truong L, Link KA, Jepsen MDE, Knutson JR, Andersen ES, Ferré-D'Amaré AR, Unrau PJ. 2021. Fluorogenic aptamers resolve the flexibility of RNA junctions using orientation-dependent FRET. *RNA* **27:** 433–444. doi:10.1261/rna.078220.120

Kabsch W. 2010. Integration, scaling, space-group assignment and post-refinement. *Acta Crystallogr D Biol Crystallogr* **66:** 133–144. doi:10.1107/S0907444909047374

Knappenberger AJ, Reiss CW, Strobel SA. 2018. Structures of two aptamers with differing ligand specificity reveal ruggedness in the functional landscape of RNA. *Elife* **7:** e36381. doi:10.7554/eLife.36381

Knappenberger AJ, Reiss CW, Focht CM, Strobel SA. 2020. A modular RNA domain that confers differential ligand specificity. *Biochemistry* **59:** 1361–1366. doi:10.1021/acs.biochem.0c00117

Lambert D, Leipply D, Shiman R, Draper DE. 2009. The influence of monovalent cation size on the stability of RNA tertiary structures. *J Mol Biol* **390:** 791–804. doi:10.1016/j.jmb.2009.04.083

Lau MW, Ferré-D'Amaré AR. 2013. An *in vitro* evolved *glmS* ribozyme has the wild-type fold but loses coenzyme dependence. *Nat Chem Biol* **9:** 805–810. doi:10.1038/nchembio.1360

Lau MW, Trachman RJ, Ferré-D'Amaré AR. 2017. A divalent cation-dependent variant of the *glmS* ribozyme with stringent $Ca^{2+}$ selectivity co-opts a preexisting nonspecific metal ion-binding site. *RNA* **23:** 355–364. doi:10.1261/rna.059824.116

Lenkeit F, Eckert I, Hartig JS, Weinberg Z. 2020. Discovery and characterization of a fourth class of guanidine riboswitches. *Nucleic Acids Res* **48:** 12889–12899. doi:10.1093/nar/gkaa1102

Leontis NB, Westhof E. 2001. Geometric nomenclature and classification of RNA base pairs. *RNA* **7:** 499–512. doi:10.1017/S1355838201002515

McCoy AJ, Grosse-Kunstleve RW, Adams PD, Winn MD, Storoni LC, Read RJ. 2007. Phaser crystallographic software. *J Appl Crystallogr* **40:** 658–674. doi:10.1107/S0021889807021206

Nakamura T, Zhao Y, Yamagata Y, Hua YJ, Yang W. 2012. Watching DNA polymerase η make a phosphodiester bond. *Nature* **487:** 196–201. doi:10.1038/nature11181

Nelson JW, Atilho RM, Sherlock ME, Stockbridge RB, Breaker RR. 2017. Metabolism of free guanidine in bacteria is regulated by a widespread riboswitch class. *Mol Cell* **65:** 220–230. doi:10.1016/j.molcel.2016.11.019

Page K, Shaffer J, Lin S, Zhang M, Liu JM. 2018. Engineering riboswitches *in vivo* using dual genetic selection and fluorescence-activated cell sorting. *ACS Synth Biol* **7:** 2000–2006. doi:10.1021/acssynbio.8b00099

Peselis A, Serganov A. 2018. *ykkC* riboswitches employ an add-on helix to adjust specificity for polyanionic ligands. *Nat Chem Biol* **14:** 887–894. doi:10.1038/s41589-018-0114-4

Petoukhov MV, Svergun DI. 2007. Analysis of X-ray and neutron scattering from biomacromolecular solutions. *Curr Opin Struct Biol* **17:** 562–571. doi:10.1016/j.sbi.2007.06.009

Porter EB, Polaski JT, Morck MM, Batey RT. 2017. Recurrent RNA motifs as scaffolds for genetically encodable small-molecule biosensors. *Nat Chem Biol* **13:** 295–301. doi:10.1038/nchembio.2278

Price IR, Gaballa A, Ding F, Helmann JD, Ke A. 2015. $Mn^{2+}$-sensing mechanisms of *yybP-ykoY* orphan riboswitches. *Mol Cell* **57:** 1110–1123. doi:10.1016/j.molcel.2015.02.016

Reiss CW, Xiong Y, Strobel SA. 2017. Structural basis for ligand binding to the guanidine-I riboswitch. *Structure* **25:** 195–202. doi:10.1016/j.str.2016.11.020

Roth A, Breaker RR. 2009. The structural and functional diversity of metabolite-binding riboswitches. *Annu Rev Biochem* **78:** 305–334. doi:10.1146/annurev.biochem.78.070507.135656

Salvail H, Balaji A, Yu D, Roth A, Breaker RR. 2020. Biochemical validation of a fourth guanidine riboswitch class in bacteria. *Biochemistry* **59:** 4654–4662. doi:10.1021/acs.biochem.0c00793

Serganov A, Nudler E. 2013. A decade of riboswitches. *Cell* **152:** 17–24. doi:10.1016/j.cell.2012.12.024

Shan S, Yoshida A, Sun S, Piccirilli JA, Herschlag D. 1999. Three metal ions at the active site of the *Tetrahymena* group I ribozyme. *Proc Natl Acad Sci* **96:** 12299–12304. doi:10.1073/pnas.96.22.12299

Sherlock ME, Breaker RR. 2017. Biochemical validation of a third guanidine riboswitch class in bacteria. *Biochemistry* **56:** 359–363. doi:10.1021/acs.biochem.6b01271

Sherlock ME, Malkowski SN, Breaker RR. 2017. Biochemical validation of a second guanidine riboswitch class in bacteria. *Biochemistry* **56:** 352–358. doi:10.1021/acs.biochem.6b01270

Sherlock ME, Sudarsan N, Breaker RR. 2018a. Riboswitches for the alarmone ppGpp expand the collection of RNA-based signaling systems. *Proc Natl Acad Sci* **115:** 6052–6057. doi:10.1073/pnas.1720406115

Sherlock ME, Sudarsan N, Stav S, Breaker RR. 2018b. Tandem riboswitches form a natural Boolean logic gate to control purine metabolism in bacteria. *Elife* **7:** e33908. doi:10.7554/eLife.33908

Shiman R, Draper DE. 2000. Stabilization of RNA tertiary structure by monovalent cations. *J Mol Biol* **302:** 79–91. doi:10.1006/jmbi.2000.4031

Trachman RJ, Draper DE. 2013. Comparison of interactions of diamine and $Mg^{2+}$ with RNA tertiary structures: similar versus differential effects on the stabilities of diverse RNA folds. *Biochemistry* **52:** 5911–5919. doi:10.1021/bi400529q

Trachman RJ, Cojocaru R, Wu D, Piszczek G, Ryckelynck M, Unrau PJ, Ferré-D'Amaré AR. 2020. Structure-guided engineering of the homodimeric mango-IV fluorescence turn-on aptamer yields an RNA FRET pair. *Structure* **28:** 776–785.e773. doi:10.1016/j.str.2020.04.007

Watson ZL, Ward FR, Meheust R, Ad O, Schepartz A, Banfield JF, Cate JH. 2020. Structure of the bacterial ribosome at 2 Å resolution. *Elife* **9:** e60482. doi:10.7554/eLife.60482

Zheng H, Cooper DR, Porebski PJ, Shabalin IG, Handing KB, Minor W. 2017. CheckMyMetal: a macromolecular metal-binding validation tool. *Acta Crystallogr D Struct Biol* **73:** 223–233. doi:10.1107/S2059798317001061